A comprehensive study on the impact of improved power materials for high-temperature thermoelectric generators[†]

Michael Bittner[1,*], Nikola Kanas[2], Richard Hinterding[1], Frank Steinbach[1], Jan Räthel[3], Matthias Schrade[4], Kjell Wiik[2], Mari-Ann Einarsrud[2], Armin Feldhoff[1,*]

[1]*Institute of Physical Chemistry and Electrochemistry, Leibniz University Hannover, DE-30167, Hannover, Germany, Fax: +49(511)762-4009; Tel: +49(511)762-3555; E-mail: michael.bittner@pci.uni-hannover.de; armin.feldhoff@pci.uni-hannover.de*
[2]*Department of Materials Science and Engineering, Norwegian University of Science and Technology, N-7491 Trondheim, Norway*
[3]*Fraunhofer-Institute for Ceramic Technologies and Systems IKTS, DE-01109 Dresden, Germany*
[4]*Department of Physics, Centre for Materials Science and Nanotechnology, University of Oslo, N-0371 Oslo, Norway*

Abstract

Dense $Ca_3Co_4O_9$-Na_xCoO_2-$Bi_2Ca_2Co_2O_9$ (CCO-NCO-BCCO) nanocomposites were produced from sol-gel derived powder by three methods: Spark plasma sintering, hot-pressing and pressureless sintering under O_2 atmosphere. The SPS processed product showed a thermoelectric power factor of 6.6 $\mu W \cdot cm^{-1} \cdot K^{-2}$ at 1073 K in air. A dense nanocomposite with all-scale hierarchical architecture and enhanced thermoelectric properties is only obtained from pressureless sintering under O_2 atmosphere. The resulting nanocomposite enables the simultaneous increase in isothermal electrical conductivity σ and Seebeck coefficient α, and it delivers a thermoelectric power factor of 8.2 $\mu W \cdot cm^{-1} \cdot K^{-2}$ at 1073 K in air. The impact of materials with enhanced electrical conductivity and power factor on the electrical power output of thermoelectric generators was verified in prototypes. A high electrical power output and power density of 22.7 mW and 113.5 mW·cm^{-2}, respectively, were obtained, when a hot-side temperature of 1073 K and a temperature difference of 251 K were applied. Different p- and n-type materials were used to verify the effect of the thermoelectric figure of merit zT and power factor on the performance of thermoelectric generators.

1. Introduction

1.1. Energy conversion - limited or infinite heat source

In the face of climate change, sustained yield and increasing power demand of the world, thermoelectric materials and their ability to directly convert heat into electrical energy can play a key role to solve recent problems. Thermoelectric oxides are applicable at high temperatures and under oxidizing conditions, allowing the recovery of waste heat from power plants and industrial processes [1]. Thermoelectricity relies on the coupling of currents of entropy I_S and electrical charge I_q in a material with each other, shown in Equation 1 [2, 3].

$$\begin{pmatrix} I_q \\ I_S \end{pmatrix} = \frac{A}{L} \cdot \begin{pmatrix} \sigma & \sigma \cdot \alpha \\ \sigma \cdot \alpha & \sigma \cdot \alpha^2 + \Lambda \end{pmatrix} \cdot \begin{pmatrix} U \\ \Delta T \end{pmatrix} \quad (1)$$

The basic transport Equation 1 can be expressed (a weak temperature dependence of the electrical chemical potential is assumed) by the electrical voltage U over the thermoelectric material of cross-sectional area A, length L, difference of temperature ΔT, the thermoelectric parameters, Seebeck coefficient α, isothermal electrical conductivity σ and the entropy conductivity at electrical open-circuit Λ. The later is related to the traditionally considered heat conductivity λ by the absolute temperature T, as given by Equation 2 [2, 3].

$$\lambda = T \cdot \Lambda \quad (2)$$

The maximum electrical power output $P_{el,max,mat}$ of p- and n-type materials is primarily determined by the power factor $\sigma \cdot \alpha^2$ (PF) and the temperature difference to the square $(\Delta T)^2$ according to Equation 3 [4, 5].

$$P_{el,max,mat} = \frac{1}{4} \cdot \frac{A}{L} \cdot \sigma \alpha^2 \cdot (\Delta T)^2 \quad (3)$$

The maximum electrical power output $P_{el,max,TEG}$ of a combination of p- ($\alpha>0$) and n-type ($\alpha<0$) materials in a thermoelectric generator (TEG) [6], can be described similarly to Equation 3 as the sum of contributions of each p- and n-type leg or by the open-circuit voltage U_{OC} to the square and the generator resistance R_{TEG}, given in Equation 4 [5].

$$P_{el,max,TEG} = \frac{1}{4} \cdot \frac{A}{L} \cdot \frac{(\Sigma \, \alpha_{p-leg} - \Sigma \, \alpha_{n-leg})^2}{(\Sigma \, \frac{1}{\sigma_{p-leg}} + \Sigma \, \frac{1}{\sigma_{n-leg}})} \cdot (\Delta T)^2$$
$$= \frac{U_{OC}^2}{4 \cdot R_{TEG}}$$
(4)

Narducci postulated the electrical power output from infinite heat sources of a thermoelectric generator can be maximized by enhancing the power factor $\sigma \cdot \alpha^2$ of the materials and keep a moderate heat conductivity λ, which is present for configuration A in Figure 1.
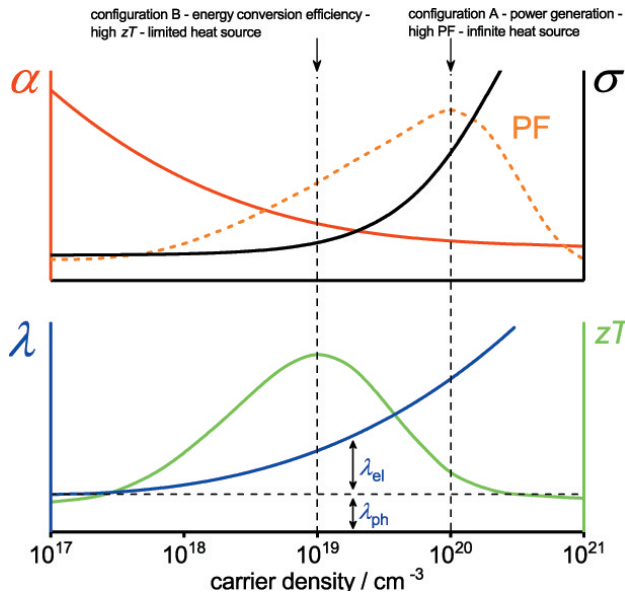

Figure 1: Thermoelectric parameters: Seebeck coefficient α, isothermal electrical conductivity σ, phononic and electrical part of the heat conductivity λ_{ph}, λ_{el}, power factor $\sigma \cdot \alpha^2$ (PF) and figure-of-merit zT as a function of the charge carrier density n. Modified from [7].

Thermoelectric materials should be designed in terms of their application areas, such as power generation from infinite or limited heat sources or at low- or high-temperatures. To improve the electrical power output of thermoelectric materials and generators, according to Equations 3-5, it is important to enhance the electrical conductivity σ and the Seebeck coefficient α. If a limited heat source is present, thermoelectric generators made of high zT materials like tellurides, illustrated in

Figure 1, with configuration B, should be used.

$$zT := \frac{\sigma \cdot \alpha^2}{\Lambda} = \frac{\sigma \cdot \alpha^2}{\lambda} \cdot T$$
(5)

The figure-of-merit zT consists of the isothermal electrical conductivity σ, the Seebeck coefficient α and the open-circuited entropy conductivity Λ. A material, which shows a high charge carrier density n and subsequently high electrical conductivity and thermoelectric power factor (configuration A), as shown in Figure 1, is superior for maximum electrical power generation, compared to a material with high figure-of-merit zT (configuration B). Accordingly, thermoelectric materials should be either optimized for maximum conversion efficiency (configuration B) or maximum electrical power generation (configuration A), since if not, working conditions for one or the other task will be suboptimal.

1.2. Concepts to improve the thermoelectric properties

The improvement of all three thermoelectric parameters is the general challenge in thermoelectrics, since these quantities are interrelated to each other by the charge carrier concentration n, indicated in Figure 1. The band structure of the materials defines the charge carrier concentration n and the charge carrier mobility μ, and changes in one of them also influence the other and thereby also σ and α [8, 9, 10]. Nanostructuring has been used to decrease the heat conductivity λ, thereby a material with an all-scale hierarchical architecture (mesoscale, nanoscale and atomic scale) would scatter phonons on each lengthscale [9, 10, 11, 12]. Recent research focuses on improving the power factor. Approaches like coherent structures with energy-matched electronic bands, carrier concentration engineering, compositionally alloyed nanostructures or band-structure engineering seem promising [13, 14, 15, 16, 17, 18]. All these research tried to solve the problem of interrelation, shown in Figure 1, between the three transport parameters σ, α and λ, which are presented as a function of the charge carrier density n, and to improve all three simultaneously. Possible processing techniques to obtain a nanostructured material are hot-pressing (HP) or spark plasma sintering (SPS) [19, 20, 21, 22, 23]. These techniques provide dense materials and are suitable for various materials, but also partly reducing it [17, 24, 25].

1.3. Oxides

The BiCuSeO oxyselenide shows competitive properties in the moderate-temperature range, compared to

alloys, half-Heusler or Zintl phase materials. However, it can hardly be considered as a real oxide and it is not stable at high temperatures and under oxidizing conditions [26, 27, 28, 29]. The $Ca_3Co_4O_9$ (CCO) oxide is a viable candidate for energy conversion at high temperatures and under oxidizing conditions from infinite heat sources, see (configuration A) Figure 1. Regarding the figure-of-merit zT, CCO can not compete with other materials, however it is non-toxic, mechanically, thermally and chemically stable in the high-temperature range in air [12, 30, 31, 32, 33]. The CCO is a layer-structured cobalt oxide and has been already investigated before [34, 35, 36]. CCO belongs to the monoclinic crystal class and forms an incommensurate, misfit-layered structure. It has a CdI_2-type CoO_2 subsystem with triangular lattice and a layered rock-salt part of three Ca_2CoO_3 units in the subsystem 2, which are stacked alternatingly along the c-axis. The b-axis parameters of the two subsystems are diverse, forming an incommensurate structure [37]. The synthesis, processing and characterization of pure CCO and triple-phase $Ca_3Co_4O_9$-Na_xCoO_2-$Bi_2Ca_2Co_2O_9$ (CCO-NCO-BCCO) nanocomposites, derived from the sol-gel technique reveals several advantages, such as grain size, homogeneity and stoichiometry, and was previously described elsewhere [5, 36].

In this work, several processing techniques like HP, SPS and pressureless O_2-sintering were used, to obtain dense triple-phase nanocomposite ceramics and improving the thermoelectric power factor and subsequently power generation [22, 25, 33, 38, 39]. The influence of these different processing techniques on the thermoelectric properties were compared, since HP and SPS are fast and partly reducing, while pressureless sintering in air and O_2, are oxidizing techniques. These dense nanocomposite ceramics were combined with recently developed, co-doped n-type indium oxides [40, 41, 42] in thermoelectric generators. The impact of high zT and high power factor materials on the electrical power output at high temperatures in air from infinite heat sources, as postulated by Narducci [43], were verified.

2. Materials and Methods

2.1. Synthesis

The p-type Na, Bi, Tb co-doped CCO and n-type $In_{2-x}O_3$ powders were synthesized via a sol-gel route, as described elsewhere [5, 36, 44]. Indium(III) nitrate 99.999 %, tin(II) acetate 95 %, aluminium(III) nitrate 99.0-102 % and germanium(IV)

ethoxide, 99.995 %, manganese(II) nitrat, 99.98 %, Zinc nitrate 99.998 % were used as sources to synthesize co-doped $Sn,Al:In_2O_3$ and $Ge,Mn,Zn:In_2O_3$, respectively. The stoichiometry, applied sintering techniques and abbreviations of synthesized samples, are shown in Table 1.

Table 1: Stoichiometry, applied sintering techniques (conventional pressureless sintering in air and O_2 (conv. Air, O_2), hot-pressing (HP)), spark plasma sintering (SPS) and abbreviations of synthesized nanocomposites (**CCO-30-35-10-Air**, **CCO-30-35-10-SPS**, **CCO-30-35-10-HP**, **CCO-30-35-10-O_2**), reference (**CCO-400-Air**) and co-doped indium oxide (**Sn,Al:In$_2$O$_3$**, **Ge,Mn,Zn:In$_2$O$_3$**) samples.

stoichiometry	sintering	abbreviation
$Ca_3Co_4O_9$	conv. Air	**CCO-400-Air**
$Ca_{2.25}Na_{0.3}Bi_{0.35}Tb_{0.1}Co_4O_9$	conv. Air	**CCO-30-35-10-Air**
$Ca_{2.25}Na_{0.3}Bi_{0.35}Tb_{0.1}Co_4O_9$	HP	**CCO-30-35-10-HP**
$Ca_{2.25}Na_{0.3}Bi_{0.35}Tb_{0.1}Co_4O_9$	SPS	**CCO-30-35-10-SPS**
$Ca_{2.25}Na_{0.3}Bi_{0.35}Tb_{0.1}Co_4O_9$	conv. O_2	**CCO-30-35-10-O_2**
$In_{1.9}Sn_{0.05}Al_{0.05}O_3$	conv. Air	**Sn,Al:In$_2$O$_3$**
$In_{1.95}Ge_{0.01}Mn_{0.01}Zn_{0.03}O_3$	conv. Air	**Ge,Mn,Zn:In$_2$O$_3$**

2.2. P-type ceramics

The p-type calcined CCO-30-35-10 powder (10 h, 1023 K) was precompressed at 200 MPa for 60 s, subsequently ground and sieved with a 100 μm mesh sieve before hot-pressing. The compacted powder was hot-pressed under vacuum in a graphite die between two Al_2O_3 plates at 1148 K for 1 h, using a pressure of 50 MPa (applied from 1023 - 1148 K) and an applied heating and cooling rate of 5 K · min^{-1}. The CCO-30-35-10 powder was processed by spark plasma sintering at 1023 K for 4 min with an applied pressure of 75 MPa. Spark plasma sintering was done using a graphite die (20 mm) in vacuum (Dr Sinter 825). The CCO-30-35-10 powder was pressed into a green body at 200 MPa using a 16 mm die and subsequently sintered under O_2 (6.0 purity from Linde) atmosphere in a tube furnace (STF 15/180 220-240V 1PH from Carbolite Gero) for 20 h at 1248 K with a flow rate of 40 mL · min^{-1} and a heating, cooling rate of 3 K · min^{-1}.

2.3. N-type ceramics

The n-type co-doped $Sn,Al:In_2O_3$ and $Ge,Mn,Zn:In_2O_3$ powders were pressed into a green body at 200 MPa using a 16 mm die and subsequently conventional pressureless sintered at 1873 K and 1573 K for 15 h in air, respectively. The green body was placed on a twisted platinum wire ($Sn,Al:In_2O_3$) [40, 42] and Sn-solder ($Ge,Mn,Zn:In_2O_3$).

2.4. Analysis of composition and properties

Phase compositions of sintered and annealed ceramics were characterized by X-ray diffraction (XRD) using a Bruker D8 Advance with Cu-K$_\alpha$ radiation. Microstructural characterization and elemental analysis of powder and ceramic samples were done by a field-emission scanning electron microscope (FE-SEM) of the type JEOL JSM-6700F, which was equipped with an energy-dispersive X-ray spectrometer (EDXS) of the type Oxford Instruments INCA 300 and a backscattered electron detector. Nanostructure was investigated by transmission electron microscopy and high-resolution TEM (HRTEM) using a JEOL JEM-2100F-UHR, which was equipped with an energy-dispersive X-ray spectrometer (EDXS) of the type Oxford Instruments INCA 300 for elemental analysis.

Density and porosity were estimated by an Archimedes setup using ISO 5018:1983 (the International Organization for Standardization) in which the dry mass, mass in solvent and wet mass of the sample, were determined. The density and porosity values were averaged from 3 measurements with less than 5 % deviation. Thermometric measurements of the mass change were done in a synthetic air and an O_2 atmosphere with a gas flow of 30 mL $\cdot$ min^{-1} and a heating rate of 5 K $\cdot$ min^{-1} within the range of 313 K to 1173 K, 1248 K, respectively, using a Netzsch STA 409 PC/PG. Ceramic samples were prepared for Hall effect measurement by painting four Au electrodes on the surfaces using a Metalor M-0034 ink, followed by an annealing step at 1123 K in air to ensure ohmic contacts. The electric properties were measured on a single sample from different treatments (HP, SPS, air, O_2), using an Agilent 34970A multichannel voltmeter and an Agilent E3642A current source. The charge carrier mobility μ and charge carrier concentration n were evaluated as described in [45].

The thermoelectric properties, isothermal electrical conductivity σ and Seebeck coefficient α of ceramic samples were carried out as a function of temperature (heated to 1073 K and measured down with equilibrium at every temperature). Samples were cut in bar shape from discs (10mm $\cdot$ 1.0mm $\cdot$ 1.0mm and 10mm $\cdot$ 2.5mm $\cdot$ 1.5mm), using a precision vertical diamond wire saw from O'Well model 3242. The power factor $\sigma \cdot \alpha^2$ was calculated from σ and α. The isothermal electrical conductivity σ was measured by a pseudo 4-point measurement, utilizing a horizontal three heating zone tube furnace from Carbolite Gero EVZ 12/450B and a home-made measurement cell. The Seebeck coefficient α was estimated with a ProboStat A setup from NorECs, the utilized furnace is an ELITE thermal system. The values were logged by KEITHLEY 2100

$6\frac{1}{2}$ Digit Multimeters. Measurement data were recorded and transduced using LAB VIEW software. Electrical measurements of σ and α were repeated with less than 5 % deviation, uncertainties of 0.1, 10 for σ, α and 20 % for the power factor were averaged from 5 values.

2.5. Assembling of thermoelectric generators

Thermoelectric generators were assembled using 10 couples of p, n-type legs (3mm x 1mm x 1mm) in a conventional generator design, shown in Figure S 10†. An Au-paste from Heraeus was used as a metallic connector. To obtain ohmic contacts, the generators CCO-30-35-10-Air/Sn,Al:In$_2$O$_3$ and CCO-30-35-10-Air/Ge,Mn,Zn:In$_2$O$_3$ were annealed at 1073 K for 4 h, the generators CCO-30-35-10-SPS/Sn,Al:In$_2$O$_3$ and CCO-30-35-10-O$_2$/Sn,Al:In$_2$O$_3$ at 973 K for 4 h in air. The thermoelectric generators were characterized using a load resistance dependent measurement under steady-state conditions at different hot-side temperatures.

3. Results and Discussion

3.1. Influence of sintering on p-types

The triple-phase CCO-NCO-BCCO nanocomposite ceramics were obtained by processing a co-doped CCO powder [5], shown in Figure 2a,b, via HP (CCO-30-35-10-HP), via SPS (CCO-30-35-10-SPS), and by O_2-sintering (CCO-30-35-10-O_2). The HP and SPS techniques are fast processing routes, which produce nanograined ceramics, which are shown in Figure 2c-f†, of a triple-phase nanocomposite.

Table 2: Lattice parameters (/ Å) of the CCO and BCCO phases of the HRTEM sites of CCO-30-35-10-O$_2$ and CCO-30-35-10-SPS nanocomposites, shown in Figure 3. Values were measured from reduced fast Fourier transformations (rFFT). Semi-coherent lattice parameters are highlighted.

| | Sites | |
	CCO-30-35-10-O$_2$	CCO-30-35-10-SPS
CCO	**a=5.35, b$_1$=2.47**, b$_2$=3.93	c=10.98 (c=10.95)
BCCO	**a=4.96, b$_1$=2.48**, c=13.27	c=16.39

The O_2-sintering is a highly oxidizing method, the sample is annealed at high temperatures for a long time, delivering an all-scale hierachical architecture, revealed in Figure 2g,h, of μm-sized grains and nanostructures. The phase composition, shown in Figure S 1† and S 2†, of powders and ceramics, processed via HP, SPS and O_2-sintering, was analyzed by XRD measurements. The CCO-30-35-10-HP and CCO-30-35-10-SPS samples show less pronounced texture compared to the
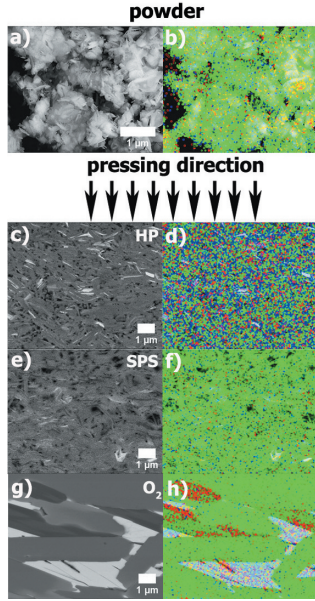
Figure 2: SEM micrographs of backscattered electrons and EDX elemental distributions of powder and cross sections: a, b) Na, Bi, Tb co-doped CCO powder, c, d) **CCO-30-35-10-HP**, e, f) **CCO-30-35-10-SPS**, g, h) **CCO-30-35-10-O$_2$**. The direction of pressing is indicated by black arrows. Phase compositions are shown in Figures S 1 and 2[†]. SEM micrographs and elemental distributions of undoped, SPS-sintered CCO ceramics and O$_2$-sintered nanocomposites are shown in Figure S 3g-j[†]. Ca-green dominates CCO phase, Na-red dominates NCO phase, Bi-blue dominates BCCO phase.

CCO-30-35-10-O$_2$ sample. Both, texture and composition can be controlled by the applied temperature during O$_2$-sintering[†]. The phase composition, revealed in Figure 2[†], and density of pure and triple-phase ceramics, given in Table 3[†], differ due to incorporated dopants and composite formation during sintering.

The density of CCO-30-35-10-HP, CCO-30-35-10-SPS and CCO-30-35-10-O$_2$ are comparable, but their micro- and nanostructure deviate, shown in Figures 2c-h and 3a-f. CCO-30-35-10-HP and CCO-30-35-10-SPS show no μm-sized grains and their nanostructure is due to the fast processing techniques forced into a certain form, indicated in Figure 3d-f. The CCO-30-35-10-O$_2$ ceramic, shown in Figure 3a-c, forms an aligned all-scale hierarchical architecture of μm-sized grains, nanostructures and point defects. Table 2 shows the lattice parameters of CCO and BCCO, calculated from reduced fast Fourier transformations of Figure 3c,f. The processing via O$_2$-sintering facilitates a dense ceramic body with highly aligned and semi-coherently CCO, NCO and BCCO 2-D nanostructures. Detailed information about elemental distribution mappings and sites of HRTEM micrographs are shown in Figures S 5-8[†].

3.2. Composition and microstructure of n-types

The phase composition, shown in Figure S 1h,i[†], and microstructure, represented in Figure S 4a-d[†], of manufactured n-type materials Sn,Al:In$_2$O$_3$ and Ge,Mn,Zn:In$_2$O$_3$ reveal homogeneously doped indium phases. The n-type Sn,Al:In$_2$O$_3$ is a dense ceramic, shown in Table 3[†]. The Ge,Mn,Zn:In$_2$O$_3$ n-type has a certain porosity, given in Table 3[†], generated while sintering on Sn-solder, which evaporated at high temperatures, causing porosity within the ceramic body.
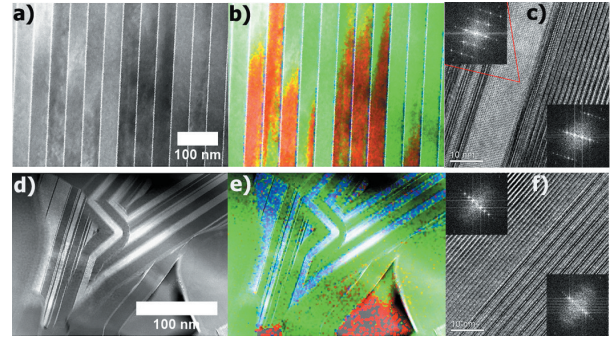

Figure 3: TEM analysis of **CCO-30-35-10-O$_2$** in a-c) and of **CCO-30-35-10-SPS** in d-f): a, d) scanning transmission electron microscopy (STEM) dark-field micrograph. b, e) EDX elemental distribution of the shown scopes, more detailed elemental distribution information is given in S 4, 6. c, f) High-resolution transmission electron microscopy (HRTEM) micrographs, more detailed information is given in S 5, 7[†]. Insets show the reduced fast Fourier transformation (rFFT). Ca-green dominates CCO phase, Na-red dominates NCO phase, Bi-blue dominates BCCO phase.

3.3. Thermoelectric properties
3.3.1. P-type ceramics

The thermoelectric transport properties, are shown in Figure 4a,b, of manufactured p- and n-type materials. The Seebeck coefficient α of CCO-30-35-10-Air and CCO-30-35-10-O$_2$ nanocomposites, shown in Figure 4a, proceeds similarly and reaches 236 and 240 μV $\cdot$ K^{-1} at 1073 K. The α values of CCO-30-35-10-SPS and CCO-30-35-10-HP nanocomposites, represented in Figure 4a, differ in trend and absolute values. Reference values for O$_2$-sintered and SPS-processed samples are given in Figure S 9a[†].

3.3.2. N-type ceramics

The Seebeck coefficient α shows similar trends for synthesized n-type materials Sn,Al:In$_2$O$_3$ and Ge,Mn,Zn:In$_2$O$_3$, revealed in Figure 4a, but also differs in absolute values and reaches 82 and 174 μV $\cdot$ K^{-1} at 1073 K, respectively. The Seebeck coefficient α of the Ge,Mn,Zn:In$_2$O$_3$ sample could be increased by Mn and Zn doping [46, 47, 48].

Table 3: Measured values of the density and porosity for CCO and nanocomposite ceramics, processed with different techniques: pressureless sintering in air (10 h: 1173 K-CCO-400-Air, 20 h: 1173 K-CCO-30-35-10-Air), O_2-sintering (20 h: 1248 K-CCO-30-35-10-O_2),HP (50 MPa, 1 h: 1148 K-CCO-30-35-10-HP), SPS (50 MPa, 4 min: 1048 K-CCO-30-35-10-SPS), and of n-type Sn,Al:In$_2$O$_3$, Ge,Mn,Zn:In$_2$O$_3$ (15 h: 1873 K and 15 h: 1573 K) using ISO 5018:1983 (the International Organization for Standardization). Values for CCO-400-Air and CCO-30-35-10-Air taken from [36, 5]. Additional values of undoped CCO and O_2 sintered nanocomposites are shown in Table S 1[†]. True density of composite ceramics is unknown.

| type	material abbreviation	bulk density / g $\cdot cm^{-3}$	true density / g $\cdot cm^{-3}$	open porosity / %	true porosity / %	closed porosity / %	theoretical density / %
p	**CCO-400-Air**	3.2 ± 0.1	4.68	33.3 ± 0.4	0.2 ± 1.1	33.5 ± 0.7	67.7 ± 1.5
p	**CCO-30-35-10-Air**	3.9 ± 0.0		19.2 ± 0.7			
p	**CCO-30-35-10-HP**	4.9 ± 0.0		0.8 ± 0.2			
p	**CCO-30-35-10-SPS**	4.9 ± 0.0		0.8 ± 0.4			
p	**CCO-30-35-10-O$_2$**	4.9 ± 0.0		3.6 ± 2.6			
n	**Sn,Al:In$_2$O$_3$**	6.6 ± 0.0	7.116	3.2 ± 2.8	7.8 ± 0.6	4.6 ± 2.2	92.2 ± 0.6
n	**Ge,Mn,Zn:In$_2$O$_3$**	5.5 ± 0.2	7.116	19.4 ± 7.8	22.3 ± 2.9	2.9 ± 6.5	77.7 ± 2.9
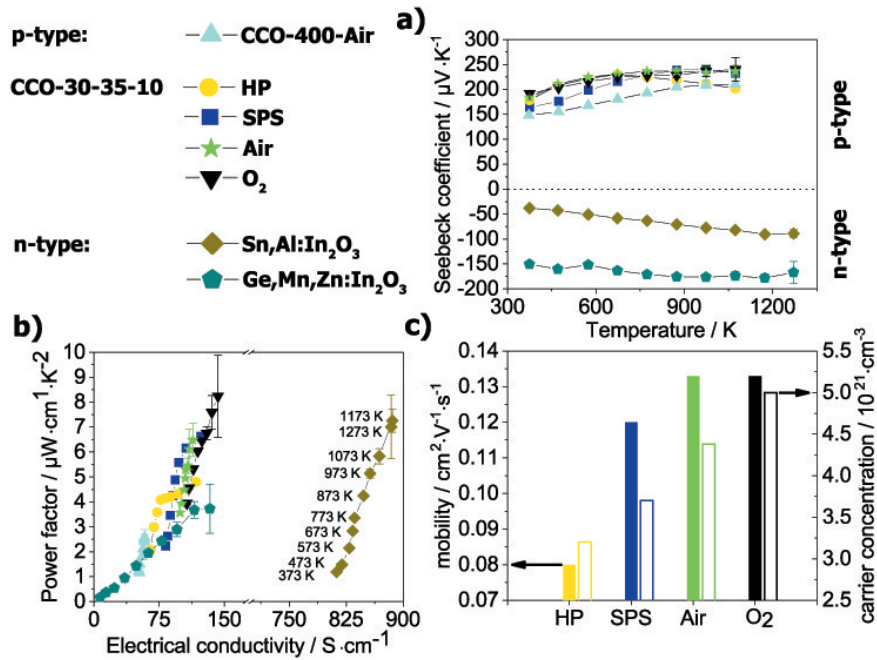
Figure 4: Thermoelectric properties as a function of temperature of **CCO-400-Air** (rectangle, turquoise, taken from [36]), **CCO-30-35-10-Air** (stars, green, taken from [5]), **CCO-30-35-10-HP** (circle, yellow), **CCO-30-35-10-SPS** (square, dark blue), **CCO-30-35-10-O$_2$** (reverse rectangle, black), **Sn,Al:In$_2$O$_3$** (diamond, dark yellow) and **Ge,Mn,Zn:In$_2$O$_3$**) (pentagon, dark green: a) Seebeck coefficient α, b) power factor $\sigma \cdot \alpha^2$ as a function of the isothermal electrical conductivity σ. c) Hall effect measurements: charge carrier mobility μ (closed bars) and charge carrier concentration n (open bars) at room temperature. Uncertainties are indicated with error bars.

3.3.3. Ioffe plot

In Figure 4b, the thermoelectric power factor $\sigma \cdot \alpha^2$ of p- and n-type materials is shown in a Ioffe plot as a function of the electrical conductivity σ [49]. The p-type materials CCO-30-35-10-Air and CCO-30-35-10-O_2 have the best combination of a high electrical conductivity σ of 116, 143 S $\cdot$ cm^{-1} and a high thermoelectric power factor $\sigma \cdot \alpha^2$ of 6.5, 8.2 μW $\cdot$ cm^{-1} $\cdot$ K^{-2} at 1073 K. The best properties of a fast processed material, shown in Figure 4b, are obtained from the CCO-30-35-10-SPS sample of 123 S $\cdot$ cm^{-1} and 6.6 μW $\cdot$ cm^{-1} $\cdot$ K^{-2}

at 1073 K. Hall effect measurements of CCO-30-35-10-HP, CCO-30-35-10-SPS, CCO-30-35-10-Air and CCO-30-35-10-O_2, as shown in Figure 4c, were carried out at room temperature. These results show simultaneous enhanced carrier mobility μ of 0.133 cm^{-2} $\cdot$ V^{-1} $\cdot$ s^{-1} and carrier concentrations n of 5 and 4.38 10^{21} $\cdot$ cm^{-3} for the CCO-30-35-10-Air, CCO-30-35-10-O_2 samples. These measurements could explain the simultaneous increase of the electrical conductivity σ and the Seebeck coefficient α in CCO-NCO-BCCO nancomposites of highly-aligned 2-D nanostructures. Measured thermoelectric

power factors of O_2-sintered and SPS-processed reference samples are given in Figure S 9b[†]. The n-type materials show a different behaviour, compared to each other. Sn,Al:In_2O_3 is a high power factor material, shown in Figure 4b [40, 50], while Ge,Mn,Zn:In_2O_3 reveals a lower thermoelectric power factor and intrinsic semiconducting behaviour.

3.3.4. Figure-of-merit zT of n-types

The heat conductivity λ, represented in Figure S 9c[†] of 2.9 W $\cdot$ m^{-1} $\cdot$ K^{-1} in the Ge,Mn,Zn:In_2O_3 sample is significantly reduced, compared to the highly electrically conducting Sn,Al:In_2O_3 sample of 11.3 W $\cdot$ m^{-1} $\cdot$ K^{-1} at 1073 K. The *zT* value of 0.1, compared to 0.056 at 1073 K, shown in Figure S 9d[†], of the Ge,Mn,Zn:In_2O_3 and Sn,Al:In_2O_3 samples, respectively, is subsequently enhanced. The course of the thermoelectric power factor, shown in Figure 4b, of Sn,Al:In_2O_3 as a function of the electrical conductivity in the Ioffe plot is more similar to the p-type materials than that of Ge,Mn,Zn:In_2O_3. For this reason, the impact of Sn,Al:In_2O_3, Ge,Mn,Zn:In_2O_3 and different p-type materials in prototypes of thermoelectric generators were estimated.

3.4. Cycle and high-temperature stability

The samples CCO-30-35-10-SPS and CCO-30-35-10-O_2, which have the highest electrical conductivity and thermoelectric power factor, were sintered either under partially reducing or oxidizing conditions, respectively. For this reason, the stability of both were estimated, shown in Figure 5a, to evaluate their applicability in a thermoelectric generator in air. Both materials show good cycle stability from 373 to 1073 K in air. However, Figure 5b,c shows that a thermal treatment for 20 h at 1173 K in air leads to a change of the phase composition of the CCO-30-35-10-SPS and CCO-30-35-10-O_2 samples. The mass change of a CCO-30-35-10-O_2 sample is shown in Figure 5b. The sample is annealed under O_2 up to 1248 K and subsequently cooled down and annealed again under air up to 1173 K, showing a small mass change. In addition, the phase compositions, shown in Figure 5c, of CCO-30-35-10-SPS and CCO-30-35-10-O_2 samples before and after exposure at 1173 K in air, were analyzed with XRD. The change of phase compositions is indicated with stars and crosses, an increased BCCO phase content for the CCO-30-35-10-SPS and NCO content within the CCO-30-35-10-O_2 sample was observed. The thermoelectric power factor as a function of the electrical conductivity, shown in the Ioffe plot of Figure 5a, remained higher for the CCO-30-35-10-O_2 sample, since the electrical conductivity

increased due to the higher NCO phase content. The thermoelectric power factors of the CCO-30-35-10-SPS and the CCO-30-35-10-O_2 samples at 1073 K, revealed in Figure 5a, were decreased by a factor of 2.23 and 1.75, after exposure for 20 h at 1173 K in air, respectively.

3.5. Thermoelectric generators - power characteristics

The p-type CCO-30-35-10-Air, CCO-30-35-10-SPS, CCO-30-35-10-O_2 and the n-type materials Sn,Al:In_2O_3 and Ge,Mn,Zn:In_2O_3 were used to build four prototypes of thermoelectric generators. The results from CCO-30-35-10-Air/Sn,Al:In_2O_3 and CCO-30-35-10-Air/Ge,Mn,Zn:In_2O_3 generators showed increased electrical power outputs if the high power Sn,Al:In_2O_3 material is used. For this reason, the p-type materials CCO-30-35-10-SPS and CCO-30-35-10-O_2 were combined with the n-type material Sn,Al:In_2O_3 in thermoelectric generators. The impact of high thermoelectric power factor and *zT* materials, on the electrical power output from infinite heat sources was estimated. A conventional design, shown in Figure S 10[†], for thermoelectric generators of 10 p/n couples was used [53, 54, 55, 56]. Figure 6a-d shows the *U-I_q* and *P-I_q* curves of the four generators at different hot-side temperatures T_{hot}.

The measured parameters like hot-side temperature T_{hot}, temperature difference ΔT, TEG resistance R_{TEG}, open-circuit voltage U_{OC}, electrical short-circuit current $I_{q,SC}$, voltage at maximum electrical power output U ($P_{el,TEG,max}$), electrical current at maximum electrical power output I_q ($P_{el,TEG,max}$), maximum electrical power output $P_{el,TEG,max}$, calculated electrical power density ω_{el} and temperature difference dependent electrical power density $\omega_{el}/(\Delta T)^2$ (active area[†]) are given in Table 4.

The highest electrical power output and electrical power density, shown in Figure 6d, of 22.7 mW and 113.5 mW$\cdot$cm^{-2}, respectively, at 1073 K hot-side temperature and 251 K temperature difference, were obtained from CCO-30-35-10-O_2 and Sn,Al:In_2O_3, which have a high electrical conductivity and thermoelectric power factor. Due to the change of phase composition at higher temperature, shown in Figure 5b,c, and a subsequently reduced thermoelectric power factor, shown Figure 5a, the generators CCO-30-35-10-SPS/Sn,Al:In_2O_3 and CCO-30-35-10-950-O_2/Sn,Al:In_2O_3 were just measured until 1073 K hot-side temperature. The generators CCO-30-35-10-Air/Sn,Al:In_2O_3 and CCO-30-35-10-Air/Ge,Mn,Zn:In_2O_3 were measured up to 1173 K hot-side temperature and delivered a maximum electrical
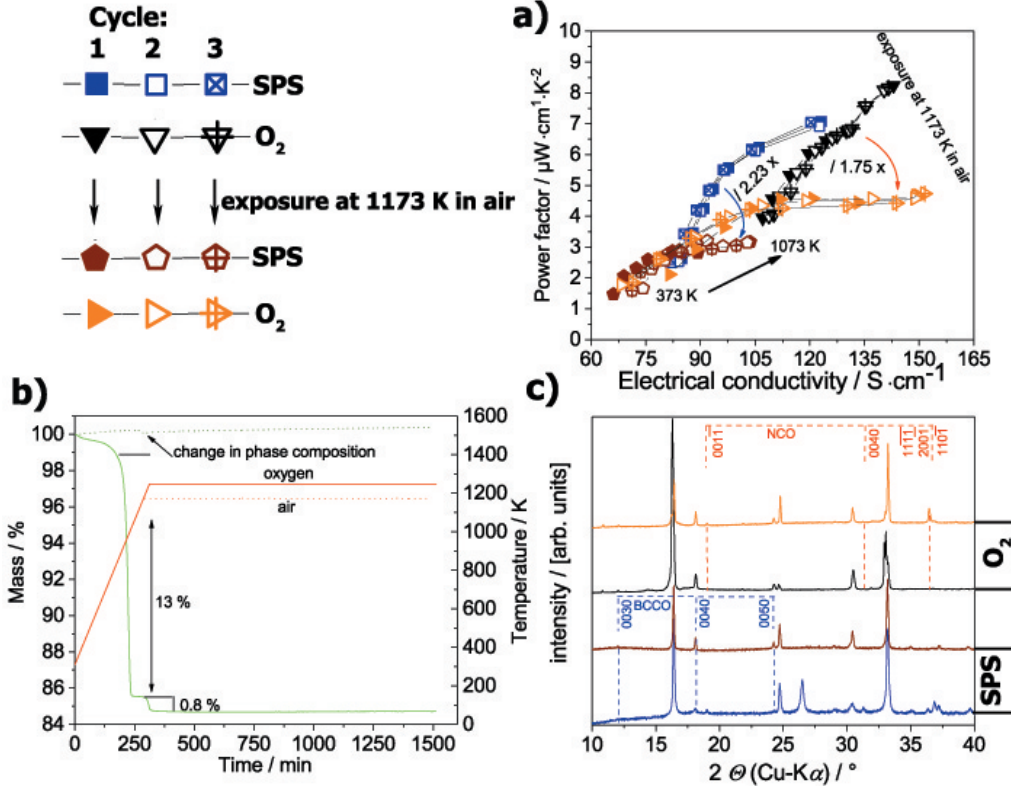
Figure 5: a) Cycle stability testing of the power factor $\sigma \cdot \alpha^2$ as a function of the isothermal electrical conductivity σ of **CCO-30-35-10-SPS** (square, pentagon) and **CCO-30-35-10-O₂** (rectangles). Closed, open and crossed symbols represent different cycles (closed - first, open - second, crossed - third cycle) before (dark blue, black) and after (brown, orange) annealing for 20 h at 1173 K in air. b) Thermogravimetry measurements of a CCO-30-35-10 sample, 20 h in O_2 (solid lines), followed by 20 h in air (dotted lines). c) X-ray diffraction patterns of CCO-30-35-10-SPS, CCO-30-35-10-O₂ before and after annealing for 20 h at 1173 K in air. Reflections of BCCO [51] and NCO [52] indicate change in phase composition.

Table 4: Measured parameters of the four thermoelectric generators (10 p/n couples) CCO-30-35-10-Air/Sn,Al:In_2O_3, CCO-30-35-10-Air/Ge,Mn,Zn:In_2O_3, CCO-30-35-10-SPS/Sn,Al:In_2O_3 and CCO-30-35-10-950-O₂/Sn,Al:In_2O_3: hot-side temperature T_{hot}, temperature difference ΔT, TEG resistance R_{TEG}, open-circuit voltage U_{OC}, electrical short-circuit current $I_{q,SC}$, voltage at maximum power output U ($P_{el,TEG,max}$), electrical current at maximum power output I_q ($P_{el,TEG,max}$), maximum electrical power output $P_{el,TEG,max}$, electrical power density ω_{el} and temperature difference dependent electrical power density $\omega_{el}/(\Delta T)^2$, both calculated from the active area of 0.2 cm^{2†}.

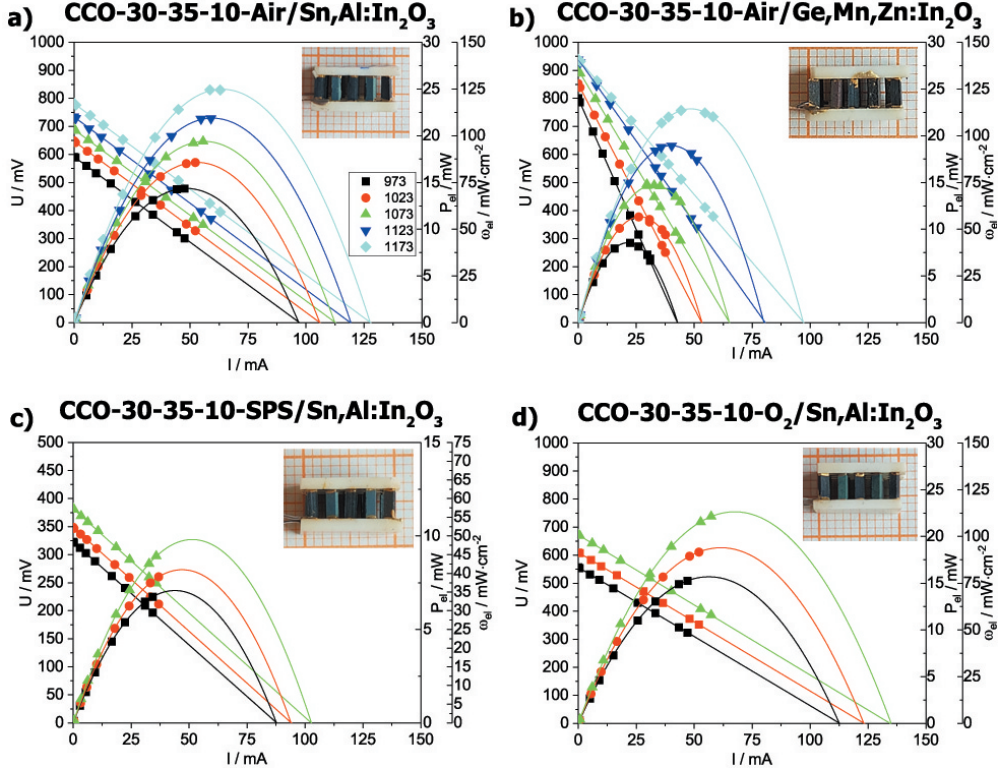| generator p/n	T_{hot} /K	ΔT /K	R_{TEG} /Ω	U_{OC} /mV	$I_{q,SC}$ /mA	U ($P_{el,max}$) /mV	I_q ($P_{el,max}$) /mA	$P_{el,max}$ /mW	ω_{el} /mW $\cdot cm^{-2}$	$\omega_{el}/(\Delta T)^2$ /μW $\cdot cm^{-2} \cdot K^{-2}$
	1173	250	6.13	782	127.5	387.7	54.2	25.0	125.0	2.00
	1123	255	6.17	735	119.0	364.0	60.0	21.8	109.0	1.68
p-CCO-30-35-10-Air/	1073	254	6.12	688	112.5	341.6	57.1	19.4	97.0	1.50
n-Sn,Al:In_2O_3	1023	249	6.14	648	105.6	317.4	53.8	17.1	85.5	1.38
	973	243	6.12	591	96.5	280.5	51.0	14.4	72.0	1.22
	1173	280	9.69	940	97.0	468.2	48.8	22.9	114.5	1.46
	1123	278	11.7	938	80.2	467.1	40.6	18.9	94.5	1.22
p-CCO-30-35-10-Air/	1073	277	13.8	902	65.3	450.6	32.9	14.7	73.5	0.96
n-Ge,Mn,Zn:In_2O_3	1023	271	16.03	853	53.2	420.9	27.2	11.4	57.0	0.78
	973	269	18.76	801	42.7	397.4	21.5	8.6	43.0	0.59
	1073	251	3.72	382	102.6	191.5	51.4	9.8	49.0	0.78
p-CCO-30-35-10-SPS/	1023	255	3.63	341	93.8	174.7	47.3	8.2	41.0	0.63
n-Sn,Al:In_2O_3	973	240	3.68	323	87.6	160.3	44.1	7.1	35.5	0.62
	1073	258	4.97	672	135.2	331.9	68.1	22.7	113.5	1.70
p-CCO-30-35-10-O₂/	1023	257	4.94	610	123.4	304.0	61.8	18.8	94.0	1.42
n-Sn,Al:In_2O_3	973	252	4.94	557	112.7	277.1	56.8	15.7	78.5	1.19

Figure 6: Characteristics of TEGs as a function of the electrical current I_q. Electrical voltage U (linear curves) and electrical power output P_{el} (parabolic curves) at different hot-side temperatures T_{hot} and as a function of the electrical current I_q of: a) CCO-30-35-10-Air/Sn,Al:In$_2$O$_3$, b) CCO-30-35-10-Air/Ge,Mn,Zn:In$_2$O$_3$, c) CCO-30-35-10-SPS/Sn,Al:In$_2$O$_3$ and d) CCO-30-35-10-O$_2$/Sn,Al:In$_2$O$_3$. Electrical power densities ω_{el} were calculated from the active area of 10 p/n couples. Generators in c and d measured until 1073 K due to limited thermal stability, shown in Figure 5.

power output and electrical power density of 25 mW, 125 mW·cm^{-2} and 22.8 mW, 114.5 mW·cm^{-2}, from 250 and 280 K temperature difference, respectively. The results of the CCO-30-35-10-SPS/Sn,Al:In$_2$O$_3$ generator remain unclear. From its thermoelectric power factor and electrical conductivity, shown in the Ioffe plot of Figure 4b, a higher electrical power output is expected. Possible explanations for this behavior could be side reactions of the p-type material with the Au-solder or an overheating of the p-type material during Au-paste solidification in the furnace. This overheating could have led to a change of phase composition, revealed in Figure 5b,c, and accordingly to decreased values in the Ioffe plot of Figure 5a. However, combinations of CCO-30-35-10-Air and CCO-30-35-10-O$_2$ with different n-type materials have much higher electrical power outputs and electrical power densities and seem to be more appropriate for thermoelectric energy conversion at high temperatures in air from infinite heat sources.

3.6. Comparison and evaluation

A comparison with other generators published in literature is difficult due to different applied hot-side temperatures, temperature differences ΔT and dimensions of used p- and n-type legs. However the calculated electrical power density ω_{el} of different generators can be compared. In this work, values of reported power density are much higher than previously reported values of 2.1, 85, and 45.3 mW·cm^{-2} [56, 57, 58] with much higher applied temperature differences. If the electrical power density is further standardized by dividing it with the applied temperature difference to the square $(\Delta T)^2$, we obtain a generator specific value of 1.7 (this work) and 0.005, 0.09, 0.18 μW · cm^{-2} · K^{-2} [56, 57, 58], which can be used to compare different generators by considering all variables, shown in Table 4. This improvement is attributed to the improved thermoelectric power factor and electrical conductivity, revealed in Figure 4b, of CCO-NCO-BCCO nanocomposites, sintered under air and O$_2$-atmosphere. Thereby, the combination of high power materials delivered the highest elec-

trical power outputs and electrical power density. The main area of application of thermoelectric oxides is energy conversion at high temperatures in air from infinite heat sources. For this application scenario, a maximized thermoelectric power factor of p- and n-type materials is much more important, than to tune the zT value [43].

4. Conclusions

A processing via O_2-sintering seems to be more promising to densify a p-type composite material than to use fast, expensive and partial reducing techniques like HP or SPS. Since the benefits of oxides are thermal and chemical stability at high temperatures, also long-term annealing is advantageous for their stability in air. Furthermore, the power factor as a function of the electrical conductivity in the Ioffe plot is more suitable than the zT value, to estimate the applicability of thermoelectric materials for energy conversion at high temperatures from infinite heat sources. The two cases of limited, or infinite heat sources should be evaluated separately, depending on the area of application. Concerning achievable figure-of-merits zT, oxides can not compete with other material classes, hence focus should be on enhancing the thermoelectric power factor. The power generation of oxide-based thermoelectric generators at high-temperatures from infinite heat sources can be maximized by designing high power materials.

5. Acknowledgment

6. References

[1] L. E. Bell, Cooling, heating, generating power, and recovering waste heat with thermoelectric systems, Science 321 (2008) 1457–1461.

[2] H. U. Fuchs, A direct entropic approach to uniform and spatially continuous dynamical models of thermoelectric devices, EHS 1(3-4) (2014) 253–265.

[3] A. Feldhoff, Thermoelectric material tensor derived from the Onsager - de Groot - Callen model, EHS 2 (1) (2015) 5–13.

[4] A. Feldhoff, Power maximum versus efficiency maximum, In preparation.

[5] M. Bittner, N. Kanas, F. Steinbach, D. Groeneveld, R. Hinterding, P. Wemhoff, K. Wiik, M.-A. Einarsrud, A. Feldhoff, Triple-phase ceramic nanocomposite with enhanced thermoelectric properties, Submitted to J. Eur. Ceram. Soc.

[6] A. Feldhoff, B. Geppert, A high-temperature thermoelectric generator based on oxides, EHS 1(1-2) (2014) 69–78.

[7] A. F. Ioffe, Semiconductor Thermoelements and Thermoelectric cooling, 1st Edition, Infosearch Ltd. London, 1957.

[8] J. R. Sootsman, D. Y. Chung, M. G. Kanatzidis, New and old concepts of thermoelectric materials, Angew. Chem. Edit. 48 (2009) 8616–8639.

[9] M. G. Kanatzidis, Nanstructured thermoelectrics: The new paradigm?, Chem. Mater. 22 (2010) 648–659.

[10] M. Martín-González, O. Caballero-Calero, P. Díaz-Chao, Nanoengineering thermoelectrics for 21st century: Energy harvesting and other trends in the field, Renew. Sust. Energ. Rev. 24 (2013) 288–305.

[11] J. Yang, H.-L. Yip, A. K.-Y. Jen, Rational design of advanced thermoelectric materials, Adv. Energy Mater. 3 (2013) 549.

[12] G. Tan, L.-D. Zhao, M. Kanatzidis, Rationally designing high-performance bulk thermoelectric materials, Chem. Rev. 116 (2016) 12123–12149.

[13] M. S. Dresselhaus, G. Chen, M. Y. Tang, R. Yang, H. Lee, D. Wang, Z. Ren, J. P. Fleurial, P. Gogna, New directions for low-dimensional thermoelectric materials, Adv. Mater. 19 (2007) 1043–1053.

[14] J. P. Heremans, B. Wiendlocha, A. M. Chamoire, Resonant levels in bulk thermoelectric semiconductors, Energ. Environ. Sci. 5 (2012) 5510–5530.

[15] Y. Pei, X. Shi, A. Lalonde, H. Wang, L. Chen, G. J. Snyder, Convergence of electronic bands for high performance bulk thermoelectrics, Nature 473 (2011) 66–69.

[16] R. J. Korkosz, T. C. Chasapis, S.-H. Lo, J. W. Doak, Y. J. Kim, C.-I. Wu, E. Hatzikraniotis, T. P. Hogan, D. N. Seidman, D. Wolverton, V. P. Dravid, M. G. Kanatzidis, High ZT in p-type $(PbTe)_{1-2x}(PbSe)_x(PbS)_x$ thermoelectric materials, J. Am. Chem. Soc. 136 (2014) 3225–3237.

[17] D. Wu, L.-D. Zhao, X. Tong, W. Li, L. Wu, Q. Tan, Y. Pei, L. Huang, J.-F. Li, Y. Zhu, M. G. Kanatzidis, J. He, Superior thermoelectric performance in PbTe-PbS pseudo-binary: extremely low thermal conductivity and modulated carrier concentration, Energ. Environ. Sci. 8 (2015) 2056–2068.

[18] C. Fu, T. Zhu, Y. Liu, H. Xie, X. Zhao, Band engineering of high performance p-type FeNbSb based half-Heusler thermoelectric materials for figure of merit zT > 1, Energ. Environ. Sci. 8 (2015) 216–220.

[19] J. Li, J. Sui, Y. Pei, C. Barreteau, D. Berardan, N. Dragoe, W. Cai, J. He, L.-D. Zhao, A high thermoelectric figure of merit ZT > 1 in Ba heavily doped BiCuSeO oxyselenides, Energ. Environ. Sci. 5 (2012) 8543–8547.

[20] F. Li, T.-R. Wei, F. Kang, J.-F. Li, Enhanced thermoelectric performance of Ca-doped BiCuSeO in a wide temperature range, J. Mater. Chem. A 1 (2013) 11942–11949.

[21] J.-L. Lan, Y.-C. Liu, B. Zhan, Y.-H. Lin, B. Zhang, X. Yuan, W. Zhang, W. Xu, C.-W. Nan, Enhanced thermoelectric properties of Pb-doped BiCuSeO ceramics, Adv. Mater. 25 (2013) 5086–5090.

[22] N. V. Nong, C.-J. Liu, M. Ohtaki, Improvement on the high temperature thermoelectric performance of Ga- doped misfit-layered $Ca_3Co_{4-x}Ga_xO_{9+\delta}$ (x=0, 0.05, 0.1, and 0.2), J. Alloy. Compd. 491 (2010) 53–56.

[23] Z. Li, C. Xiao, S. Fan, Y. Deng, W. Zhang, B. Ye, Y. Xie, Dual vacancies: An effective strategy realizing synergistic optimization of thermoelectric property in BiCuSeO, J. Am. Chem. Soc. 137 (2015) 6587–6593.

[24] C. Barreteau, D. Berardan, L. Zhao, N. Dragoe, Influence of Te substitution on the structural and electronic properties of thermoelectric BiCuSeO, J. Mater. Chem. A 1 (2013) 2921–2926.

[25] J. G. Noudem, D. Kenfaui, D. Chateigner, M. Gomina, Toward the enhancement of thermoelectric properties of lamellar $Ca_3Co_4O_9$ by edge-free spark plasma texturing, Scripta Mater. 66 (2012) 258–260.

[26] J. Sui, J. Li, J. He, Y.-L. Pei, D. Berardan, H. Wu, N. Dragoe, W. Cai, L.-D. Zhao, Texturation boosts the thermoelectric performance of BiCuSeO oxyselenides, Energ. Environ. Sci. 6 (2013) 2916–2920.

[27] Y. Liu, L.-D. Zhao, Y. Zhu, Y. Liu, F. Li, M. Yu, D.-B. Liu, W. Xu, Y.-H. Lin, C.-W. Nan, Synergistically optimizing electrical and thermal transport properties of BiCuSeO via a dual-doping approach, Adv. Energy Mater. 6 (2016) 1502423.

[28] G.-K. Ren, S.-Y. Wang, Y.-C. Zhu, K. J. Ventura, X. Tan, W. Xu, Y.-H. Lin, J. Yang, C.-W. Nan, Enhancing thermoelectric performance in hierarchically structured BiCuSeO by increasing bond covalency and weakening carrier-phonon coupling, Adv. Energy Mater.

[29] C. Barreteau, D. Berardan, N. Dragoe, Studies on the thermal stability of BiCuSeO, J. Solid State Chem. 222 (2015) 53–59.

[30] Y.-L. Pei, H. Wu, D. Wu, F. Zheng, J. He, High thermoelectric performance realized in a BiCuSeO system by improving carrier mobility through 3D modulation doping, J. Am. Chem. Soc. 136 (2014) 13902–13908.

[31] D. M. Rowe, CRC Handbook of Thermoelectrics, 89th Edition, CRC Press, Boca Raton, FL, 1995.

[32] M. Ohtaki, K. Araki, K. Yamamoto, High thermoelectric performance of dually doped ZnO ceramics, J. Electron. Mater. 38 (2009) 1234–1238.

[33] N. V. Nong, N. Pryds, S. Linderoth, M. Ohtaki, Enhancement of the thermoelectric performance of p-type layered oxide $Ca_3Co_4O_{9+\delta}$ through heavy doping and metallic nanoinclusions, Adv. Mater. 23 (2011) 2484–2490.

[34] G. Xu, R. Funahashi, M. Shikano, I. Matsubara, Y. Zhou, Thermoelectric properties of the Bi- Na-substituted $Ca_3Co_4O_9$ system, Appl. Phys. Lett. 80 (2002) 3760–3762.

[35] Y. Miyazaki, Crystal structure and thermoelectric properties of the misfit-layered cobalt oxides, Solid State Ionics 172 (2004) 463–467.

[36] M. Bittner, L. Helmich, F. Nietschke, B. Geppert, O. Oeckler, A. Feldhoff, Porous $Ca_3Co_4O_9$ with enhanced thermoelectric properties derived from sol-gel synthesis, J. Eur. Ceram. Soc. 37 (2017) 3909–3915.

[37] Y. Miyazaki, M. Onoda, T. Oku, M. Kikuchi, Y. Ishii, Y. Ono, Y. Morii, T. Kajitani, Modulated structure of thermoelectric compound $[Ca_2CoO_3]$ CoO_2, J. Phys. Soc. Jpn. 71 (2002) 491–497.

[38] L. Xu, F. Li, Y. Wang, High-temperature transport and thermoelectric properties of $Ca_3Co_{4-x}Ti_xO_9$, J. Alloy. Compd. 501 (2010) 115–119.

[39] Y. Wang, Y. Sui, P. Ren, L. Wang, X. Wang, W. Su, H. Fan, Strongly correlated properties and enhanced thermoelectric response in $Ca_3Co_{4-x}M_xO_9$ (M = Fe, Mn, and Cu), Chem. Mater. 22 (2010) 1155–1163.

[40] D. Bérardan, E. Guilmeau, A. Maignan, B. Raveau, Enhancement of the thermoelectric performances of In_2O_3 by the coupled substitution of M^{2+}/Sn^{4+} for In^{3+}, J. Appl. Phys. 104 (2008) 064918–1–064918–5.

[41] Y. L. Yan, Y. X. Wang, Electronic structure and low temperature thermoelectric properties of $In_{24}M_8O_{48}$ (M=Ge^{4+}, Sn^{4+},Ti^{4+}, and Zr^{4+}), J. Comput. Chem. 33 (2012) 88–92.

[42] E. Guilmeau, D. Bérardan, C. Simon, A. Maignan, B. Raveau, D. Ovono Ovono, F. Delorme, Tuning the transport and ther-

moelectric properties of In_2O_3 build ceramics through doping at In-site, J. Appl. Phys. 106 (2009) 053715–1–053715–7.

[43] D. Narducci, Wo we really need highthermoelectric figure of merit? a critical appraisal to the power conversion efficiency of thermoelectric materials, Appl. Phys. Lett. 99 (2011) 102104–1–102104–3.

[44] M. Bittner, B. Geppert, N. Kanas, S. P. Singh, K. Wiik, A. Feldhoff, Oxide-based thermoelectric generator for high-temperature application using p-type $Ca_3Co_4O_9$ and n-type $Ca_{1.95}Sn_{0.05}O_3$ legs, EHS 3(3) (2016) 213–222.

[45] M. Schrade, T. Norby, T. G. Finstad, Hall effect measurements on themoelectric $Ca_3Co_4O_9$: On how to determine the charge carrier concentration in strongly correlated misfit cobaltites, J. Appl. Phys. 117 (2015) 205103–1–205103–6.

[46] M. Košir, M. Podlogar, N. Daneu, A. Rečnik, E. Guilmeau, S. Bernik, Phase formation, microstructure development and thermoelectric properties of $(ZnO)_kIn_2O_3$ ceramics, J. Eur. Ceram. Soc. 37 (2017) 2833–2842.

[47] S. K. S. R. Sarath Kumar, Transparent ITO-Mn:ITO thin-film thermocouples, IEEE Sens. J. 9 (2009) 809–813.

[48] M. Ohtaki, D. Ogura, K. Eguchi, H. Arai, High-temperature thermoelectric properties of In_2O_3-based mixed oxides and their applicability to thermoelectric power generation, J. Mater. Chem. 4(5) (1994) 653–656.

[49] Q. Zhu, E. M. Hopper, B. J. Ingram, T. O. Mason, Combined jonker and ioffe analysis of oxide conductors and semiconductors, J. Am. Ceram. Soc. 94 (2011) 187–193.

[50] E. Guilmeau, D. Bérardan, C. Simon, A. Maignan, B. Raveau, D. O. Ovono, F. Delorme, Tuning the transport and thermoelectric properties of In_2O_3 bulk ceramics through doping at In-site, J. Appl. Phys. 106 (2009) 053715–1–053715–7.

[51] E. Guilmeau, M. Pollet, D. Grebille, M. Hervieu, M. Muguerra, R. Cloots, M. Mikami, R. Funahashi, Nanoblock coupling effect in iodine intercalated $[Bi_{0.82}CaO_2]_2[CoO_2]_{1.69}$ layered cobaltite, Inorg. Chem. 46 (2007) 2124–2131.

[52] L. Viciu, J. W. G. Bos, H. W. Zandbergen, Q. Huang, M. L. Foo, S. Ishiwata, A. P. Ramirez, M. Lee, N. P. Ong, R. J. Cava, Crystal structure and elementary properties of Na_xCoO_2 (x = 0.32, 0.51, 0.6, 0.75, and 0.92) in the three-layer $NaCoO_2$ familiy, Phys. Rev. B 73 (2006) 174104–1–174104–10.

[53] X. Hu, P. Jood, M. Ohta, M. Kunii, K. Nagase, H. Nishiate, M. G. Kanatzidis, A. Yamamoto, Power generation from nanostructured PbTe-based thermoelectrics: comprehensive development from materials to modules, Energ. Environ. Sci. 9 (2016) 517–529.

[54] S. M. Choi, K. H. Lee, C. H. Lim, W. S. Seo, Oxide-based thermoelectric power generation module using p-type $Ca_3Co_4O_9$ and n-type $(ZnO)_7In_2O_3$ legs, Energ. Convers. Manage. 52 (2011) 335–339.

[55] K. Park, G. W. Lee, Fabrication and thermoelectric power of Π-shaped $Ca_3Co_4O_9/CaMnO_3$ modules for renewable energy conversion, Energy 60 (2013) 87–93.

[56] L. Han, Y. Jiang, S. Li, H. Su, X. Lan, K. Qin, T. Han, H. Zhong, L. Chen, D. Yu, High temperature thermoelectric properties and energy transfer devices of $Ca_3Co_{4-x}Ag_xO_9$ and $Ca_{1-y}Sm_yMnO_3$, J. Alloys Compd. 509 (2011) 8970–8977.

[57] S. Urata, R. Funahashi, T. Mihara, A. Kosuga, S. Sodeoka, T. Tanaka, Power generation of a p-type $Ca_3Co_4O_9$/n-type $CaMnO_3$ module, Int. J. Appl. Ceram. Technol. 4 (2007) 535–540.

[58] N. V. Nong, N. Pryds, Nanostructured oxide materials and modules for high-temperature power generation from waste heat, Adv. Nat. Sci. : Nanosci. Nanotechnol. 4 (2013) 023002.